WILEY-VCH

DOI: 10.1002/((please add manuscript number))
Article type: Communication

Enhanced Photocatalytic H_2 Production in Core-Shell Engineered Rutile TiO_2

Yongqiang Yang, Gang Liu, John TS Irvine, Hui-Ming Cheng**

Mr Y. Q. Yang
Department of Materials Science and Technology, School of Chemistry and Materials Science, University of Science and Technology of China, 96 Jinzhai Road , HeFei 230026 , China

Mr Y. Q. Yang, Prof. G. Liu, Prof. H. M. Cheng
Shenyang National Laboratory for Materials Science, Institute of Metal Research, Chinese Academy of Sciences, 72 Wenhua Road, Shenyang 110016, China
E-mail: gangliu@imr.ac.cn (GL); cheng@imr.ac.cn (HMC)

Prof. J. TS Irvine
School of Chemistry, University of St. Andrews, Fife, KY16 9ST, UK

Keywords: TiO_2, Photocatalyst, Hydorgen, Core-shell

Semiconductor photocatalysis is an attractive approach to efficient solar energy conversion, reliant on appropriately engineered band structures to promote surface reactions under light irradiation. There are three fundamental factors for consideration in the design and development of semiconductor photocatalysts: (i) light absorption, (ii) separation and transport of photogenerated electrons and holes in bulk, and (iii) their transfer on the surface.[1-5] As a quintessential example of semiconductor photocatalysts, transition metal oxides and nitrides, in which valence band maxima and conduction band minima consists of anionic *p* states and cationic *d* states, respectively, always suffer from the much smaller mobility of holes in the valence band than electrons in the conduction band due to the intrinsically smaller slope of *p* states than *d* states at the extrema.[6-9] Under light irradiation, this imbalance could lead to a larger population or a higher probability of surface-reaching electrons than that of holes. As a consequence, the photocatalytic activity is largely compromised because most photocatalytic reactions, including hydrogen release from water splitting or a water/electron scavenger mixture, are controlled by (multi)holes involved in

oxidizing half reactions.[10,11] Past efforts to address this challenge have mainly focused on improving the transfer of holes on the surface in factor (iii), for example, by co-catalyst loading,[10,12] photocatalyst faceting,[13] surface hydrogenated disordering,[14-16] and developing alternative reaction mechanisms, *e.g.* redox shuttle mechanism.[17] On the other hand, while an important approach to improving photocatalytic activity, modulating the probabilities of electrons and holes reaching the surface in factor (ii) has been overlooked.

Considering the fact that the mobility of charge carriers is dominantly controlled by their effective masses, which are intrinsically sensitive to the crystal structures of the materials, there seems little room to directly change the probabilities of electrons and holes reaching the surface of photocatalysts with given crystal structures. One possible solution is to create unique band alignments through the interior to the surface of a particle to regulate the transport of electrons and holes. As shown in **Fig. 1**, the proposed band alignments of a particle consist of an anion vacancy-containing crystalline core and an amorphous shell, enabling the suppression of the transport of conduction band electrons while facilitating the transport of valence band holes by the upward onsets of the band edges at the core/shell interface. Herein, we demonstrate the proposed band alignment modulation in rutile TiO_2, the most thermodynamically stable TiO_2 polymorph and a widely used model photocatalyst. We attain a crystalline Ti^{3+} core/amorphous Ti^{4+} shell structure through a two-step hierarchically discrete modification combining thermal reduction and hydrothermal fluorination. This process turns the almost photocatalytically inactive commercial rutile TiO_2 microsize crystals into an efficient photocatalyst for hydrogen production from a mixture of water and methanol. The average hydrogen evolution rate is improved by over 100 folds from 1.7 to 268.3 μmol h^{-1} by modulating band structure as a result of the created core/shell structure. This significant improvement is attributed to the key role of the unusual core/shell structure in populating many more surface-reaching holes than electrons by regulating their transport behaviors from the interior to the surface under irradiation.

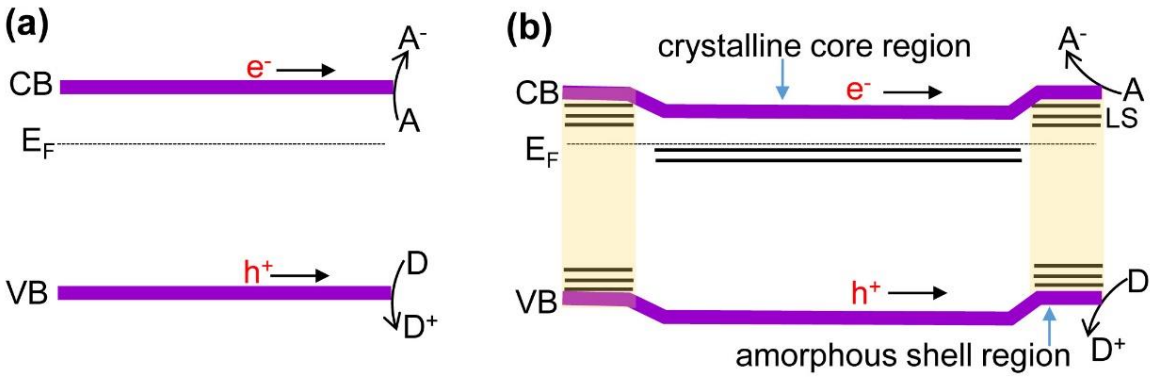

Figure 1 Transports of photogenerated electrons and holes in two different band alignments. The band alignments of an n-type semiconductor photocatalyst (a) without and (b) with a crystalline core containing anion vacancies and an amorphous shell. CB, conduction band; VB, valence band; LS, localized states; E_F: Fermi level; A: electron acceptor; D: electron donor.

The challenge of sample preparation lies in introducing an amorphous structure in a highly crystalline particle. It is well established that thermal treatment in a reductive atmosphere such as hydrogen usually leads to the generation of anion vacancies and related cations with lower oxidation states in reduced crystalline materials, for example, oxygen vacancies balanced by Ti^{3+} cations in reduced TiO_2.[18] The continuous loss of lattice atoms makes it possible to disrupt the long-range atomic order and form an amorphous structure. However, a dilemma arises here because the thermal treatment itself can also induce recrystallization of the reduced materials with a large loss of atoms to form new crystalline materials, for example, Ti_2O_3 from reduced TiO_2. Therefore, it is unlikely to create both a surface amorphous structure and bulk Ti^{3+} in TiO_2 in a reductive atmosphere by the common thermal treatment method as this is prevented by the tradeoff between the formation of Ti^{3+} defects and recrystallization.

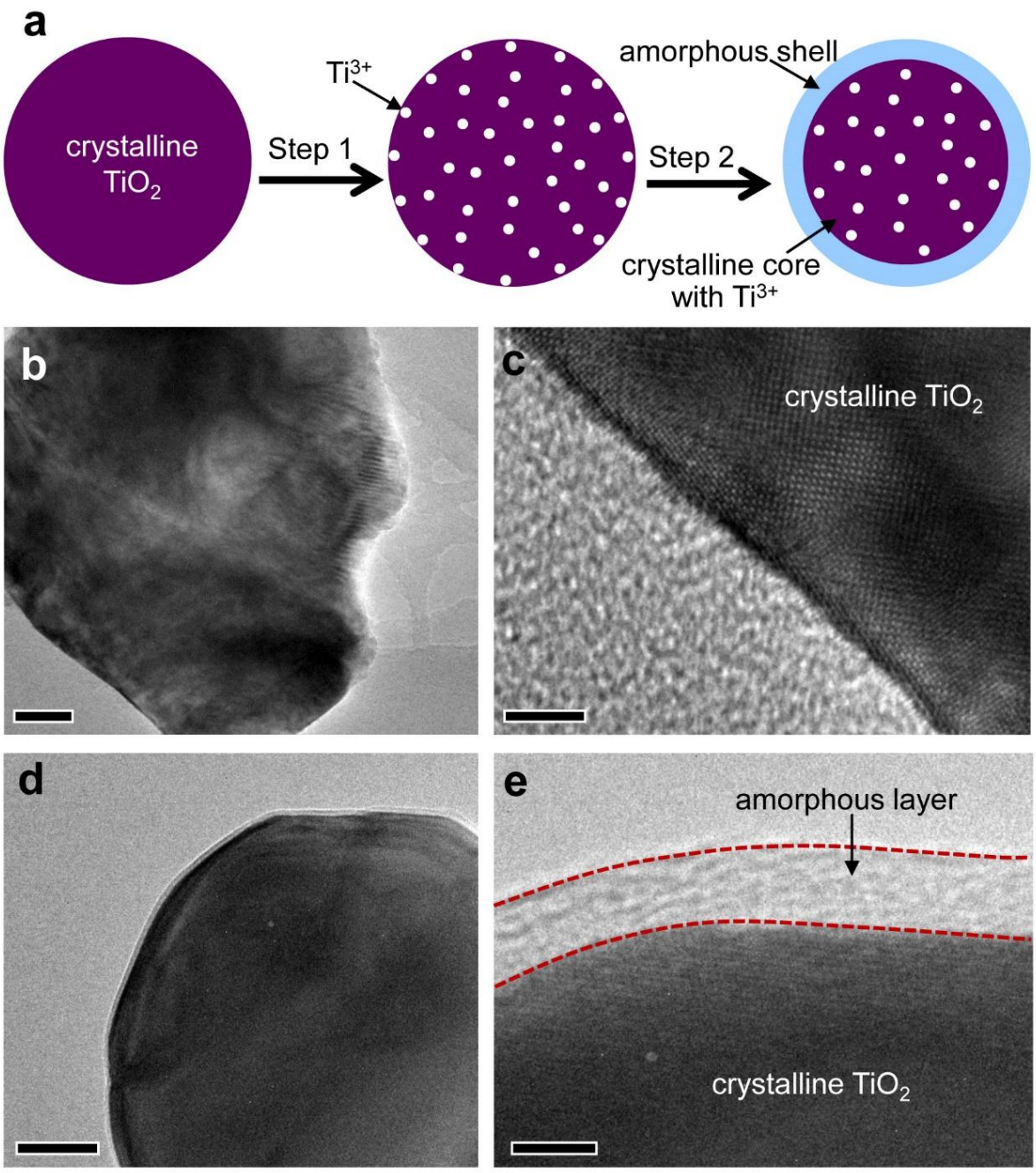

Figure 2 Formation of a crystalline Ti^{3+} core/amorphous Ti^{4+} shell structured TiO_2 particle. (**a**), Schematic of the formation of a crystalline Ti^{3+} core/amorphous Ti^{4+} shell TiO_2 particle from a crystalline TiO_2 particle by a two-step treatment. In Step 1, oxygen is lost and Ti^{3+} created in the whole particle of pristine crystalline TiO_2 in a reductive atmosphere of hydrogen gas (The sample obtained after Step 1 is denoted **TiO_2 with Ti^{3+}**). In step 2, the Ti^{3+} containing surface layer is converted into an amorphous layer by hydrothermally treating the TiO_2 with Ti^{3+} in a hydrofluoric acid solution, with the surviving Ti^{3+} preserved in the core

(The sample obtained after Step 2 is denoted **TiO_2 with Ti^{3+} & AL**, where AL means the amorphous layer). The reference sample of crystalline/amorphous core/shell TiO_2 without Ti^{3+} obtained using only Step 2 is denoted **TiO_2 with AL**. Transmission electron microscope (TEM) images of (**b**) TiO_2 and (**d**) TiO_2 with Ti^{3+} & AL. (**c**) and (**e**), High magnification TEM images of the typical edge areas of the samples (**b**) TiO_2 and (**d**) TiO_2 with Ti^{3+} & AL. Scale bars in (**b**-**e**) are 50 nm, 5 nm, 50 nm and 3 nm, respectively.

By taking advantage of its strong corrosivity, a hydrothermal fluorination process in hydrofluoric acid was used to create an amorphous surface layer on TiO_2. To achieve an amorphous surface together with Ti^{3+} defects in TiO_2, thermal reduction followed by hydrothermal fluorination, as shown in **Fig. 2**a, was developed to activate commercial rutile TiO_2 microcrystals. Figs. 2b and c give typical TEM images of the TiO_2 particle before the two step treatments, showing clear lattice structures both in the bulk and at the edge of the particle with high crystallinity. In contrast, a uniform amorphous layer with the thickness of around 3 nm (Figs. 2d and e) was formed in TiO_2 with Ti^{3+}&AL obtained by treating TiO_2 with the two-step process. Two reference samples, TiO_2 with Ti^{3+} and TiO_2 with AL obtained by treating TiO_2 only with thermal reduction and hydrothermal fluorination, respectively, show distinctly different microstructures in terms of the surface amorphous layer (**Fig. S1**). Moreover, TiO_2 with Ti^{3+} does not give a very clear lattice atom image, probably because of the presence of disordered defects. It is noted that all samples show almost identical X-ray diffraction patterns to that of pristine rutile TiO_2 and no formation of any other phase was observed after the treatments (**Fig. S2**).

X-ray photoelectron spectroscopy (XPS) was used to determine the compositions of, and chemical states in, the surface layers of the samples. High resolution XPS spectra of TiO_2 with Ti^{3+}&AL (**Fig. 3**a) show Ti 2*p*, O 1*s* and F 1*s* core electron peak regions. The binding energy of Ti 2*p* electrons (Ti $2p_{3/2}$, 458.4 eV; Ti $2p_{1/2}$, 464.2 eV) is exclusively assigned to

Ti^{4+} and no signal of Ti^{3+} was detected in the surface layer. The major and minor peaks at 529.8 eV and 532.1 eV in the O 1*s* spectrum are attributed to O in Ti-O bonds and surface hydroxyl groups, respectively. Compared to TiO_2 (**Fig. S3**), the binding energy of both Ti 2*p* and O 1*s* electrons in TiO_2 with Ti^{3+}&AL is shifted to a lower energy by around 0.4 eV, largely because of the presence of fluorine species in the amorphous surface layer. The presence of fluorine in the form of Ti-F bonds is indicated by the strong F 1*s* peak at 684.2 eV.[19] The atomic ratio of F to Ti is determined to be 3:20. These results suggest that the amorphous surface layer of TiO_2 with Ti^{3+}&AL consists of Ti, O and F and is free of Ti^{3+} defects. On the other hand, the presence of Ti^{3+} defects in TiO_2 with Ti^{3+}&AL was confirmed by electron spin resonance (ESR) spectroscopy. The ESR spectrum in Fig. 3b shows a peak centered at g = 1.993, assigned Ti^{3+} in the bulk created by reduction ($2\,Ti_{Ti}^{x} + O_O^x \rightarrow 2\,Ti_{Ti}^{/} + V_O^{\bullet} + {}^1/_2\,O_2$),[20,21] in TiO_2 with Ti^{3+}&AL. The fact that it has a lower intensity than TiO_2 with Ti^{3+} can be explained due to the quenching of Ti^{3+} in the surface layer when TiO_2 with Ti^{3+} was hydrothermally treated in hydrofluoric acid to create the amorphous surface layer. This is also the reason why no Ti^{3+} signal was detected by XPS in the amorphous surface layer of TiO_2 with Ti^{3+}&AL because of the very limited detection depth (1-10 atomic layers for inorganic materials). On the basis of these results, together with features of the thermal reduction and subsequent hydrothermal fluorination involved in the preparation of TiO_2 with Ti^{3+}&AL, one can reasonably infer that the Ti^{3+} surviving from the hydrothermal fluorination step is mainly located in the crystalline core to form the crystalline Ti^{3+} core/amorphous Ti^{4+} shell structure, as illustrated in the right panel of Fig. 2a.

The light absorption and band edges of photocatalysts are important properties that affect their performance. Introducing a fluorine-modified amorphous surface layer and/or Ti^{3+} did not change the intrinsic absorption edge and thus the bandgap of rutile TiO_2 as indicated by Fig. S4 because of the deeper energy level of F 2*p* than O 2*p* in the valence band region and

location of Ti^{3+}-related localized states mostly at 0.75-1.18 eV below the bottom of conduction band.[22,23] The additional broad absorption band beyond 450 nm from both TiO_2 with Ti^{3+}&AL and TiO_2 with Ti^{3+} is caused by the low energy photon or thermal excitations of these Ti^{3+}-related localized states. The flat band potentials of the samples were studied by Mott-Schottky (MS) plots (**Fig. 3**c). All the samples show a typical n-type nature in their MS curves with negative slopes. Both TiO_2 with AL and TiO_2 with Ti^{3+}&AL have nearly identical flat band potentials of around 0.06 V to TiO_2, while the TiO_2 with Ti^{3+} has a cathodically shifted potential close to 0 V as a result of the Ti^{3+}-containing surface layer. This Ti^{3+} modulated flat band potential shift plays a crucial role in improving the photocatalytic performance by regulating the transport and transfer behavior of charge carriers, as will be demonstrated later.

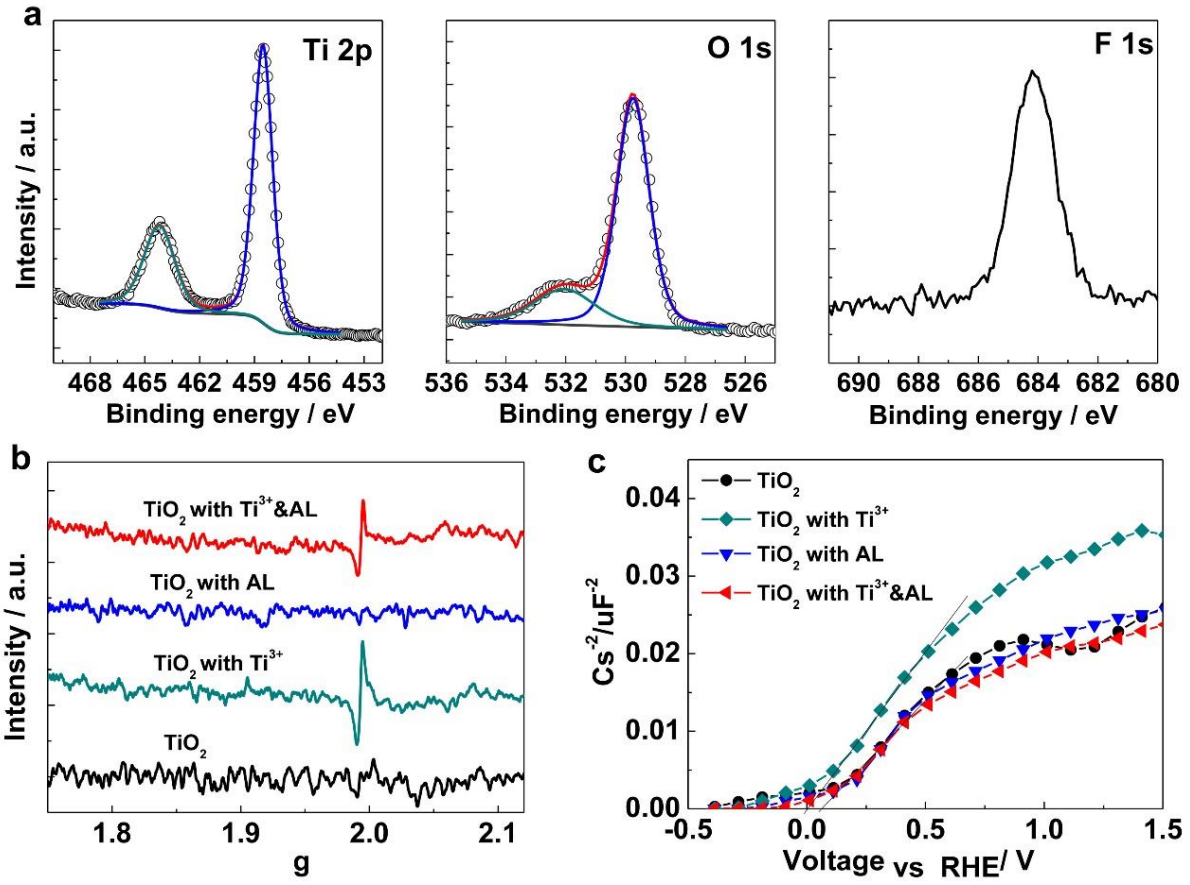

Figure 3 Composition, chemical state and flat band potential analysis. (**a**), High resolution X-ray photoelectron spectra of Ti 2*p*, O 1*s* and F 1*s* core electron level peak

regions of TiO_2 with Ti^{3+}&AL. (**b**), Electron spin resonance spectra of TiO_2, TiO_2 with Ti^{3+}, TiO_2 with AL, and TiO_2 with Ti^{3+}&AL. (**c**), Mott-Schottky plots of the four samples measured in the dark. Measurements were conducted in a 0.2 M Na_2SO_4 solution at room temperature.

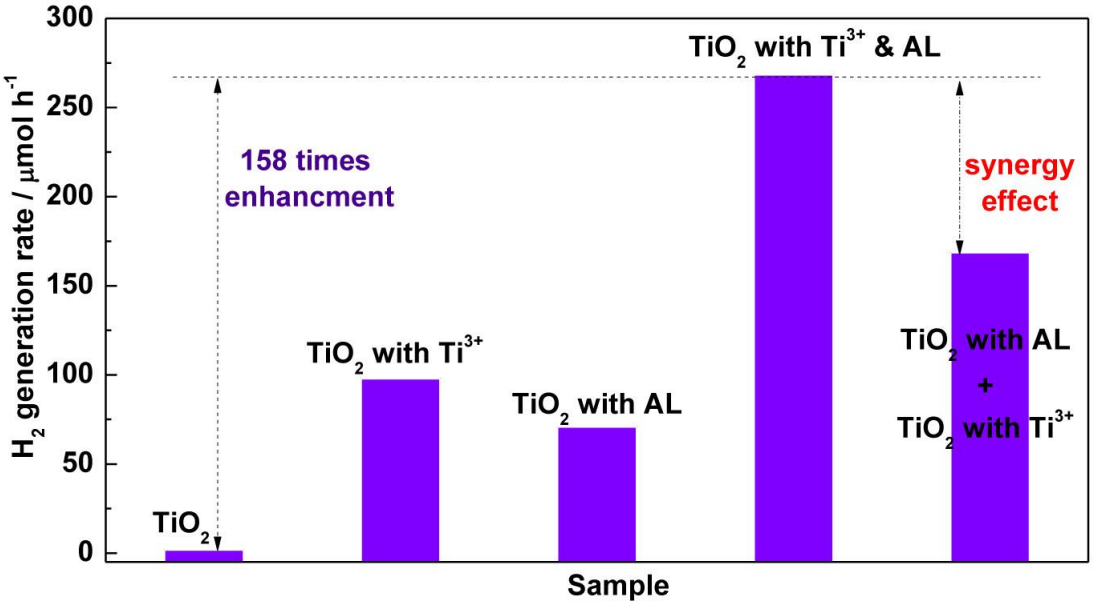

Figure 4 Comparisons of the average photocatalytic hydrogen generation rates of the four rutile TiO_2 photocatalysts. Photocatalytic hydrogen generation of the four rutile TiO_2 photocatalysts from an aqueous solution containing 10 vol% methanol as an electron donor as a function of UV-visible light irradiation time. All photocatalysts were loaded with 1 wt% Pt as a co-catalyst prior to the photocatalytic hydrogen generation tests.

Rutile TiO_2 is usually considered to be a less active photocatalyst for hydrogen evolution from the water-splitting half reaction because of its thermodynamically unfavorable conduction band bottom close to the redox potential of H^+/H_2.[3,24] However, the photocatalytic hydrogen evolution reactions suggest that the rutile TiO_2 with Ti^{3+}&AL loaded with a Pt co-catalyst can be an active photocatalyst for hydrogen evolution from an aqueous solution containing methanol as electron donor under UV-visible light. As shown in Fig. 4, TiO_2 with Ti^{3+}&AL gives a significantly improved photocatalytic activity in hydrogen

evolution compared with the other three reference samples TiO_2, TiO_2 with AL, and TiO_2 with Ti^{3+}. The average hydrogen evolution rate is enhanced from 1.7 for TiO_2 to 268.3 μmol h^{-1} for TiO_2 with Ti^{3+}&AL. The enhanced hydrogen evolution activity of TiO_2 with Ti^{3+}&AL is higher by 99.7 μmol h^{-1} than the sum of the activities of TiO_2 with Ti^{3+} and TiO_2 with AL, clearly suggesting the presence of an obvious synergistic effect between Ti^{3+} core and AL shell. Moreover, TiO_2 with Ti^{3+}&AL has good stability as demonstrated in the cyclic tests (**Fig. S5**). A control experiment, where both the amorphous surface layer and Ti^{3+} of sample TiO_2 with Ti^{3+}&AL were removed by heating sample in air (**Figs. S6 and 7**), made the photocatalyst almost inactive again. It is noted that all four samples studied have comparable specific surface areas (2.5 m^2g^{-1} for TiO_2, 1.8 m^2g^{-1} for TiO_2 with Ti^{3+}, 2.0 m^2g^{-1} for TiO_2 with AL, and 1.6 m^2g^{-1} for TiO_2 with Ti^{3+} & AL) and also close particle sizes, ruling out the possible contribution of surface area or particle size changes to the observed activity enhancement. Therefore, the significant performance enhancement is the result of the regulated transport of electrons and holes in bulk and also abundant catalytic active sites produced by the crystalline/amorphous core/shell structure will be confirmed in the following sections. Photocatalytic hydrogen evolution for TiO_2 with Ti^{3+}&AL and TiO_2 with Ti^{3+} under visible light ($\lambda > 420$ nm) is negligible, although there is strong absorption in the visible light range for both samples. This is consistent with the previous reports.[18,25]

To understand the origin of the activated photocatalytic hydrogen evolution of rutile TiO_2, the fates of the photogenerated charge carriers in different samples were studied by photoelectrochemical (PEC) spectroscopy under chopped light irradiation (**Figs. 5**a and b) and Mott-Schottky spectroscopy in the dark and under light irradiation (**Figs. 5**c and d). The films of four TiO_2 samples supported on fluorine doped tin oxide (FTO) glass substrates as photoanodes have similar microstructures and close film thicknesses (**Fig. S8 and 9**). The films also show similar optical absorption spectra to their counterparts in powder (**Fig. S10**). The PEC water oxidation reaction occurring on a photoanode induced by the photogenerated

holes is accompanied by the flow of photogenerated electrons through an external circuit to generate photocurrent. The decay behavior of the photocurrent after switching the light on/off together with the photocurrent density can be a good indicator of the fates of photogenerated charge carriers in the photoanode. Consistent with the much superior photocatalytic hydrogen evolution of TiO_2 with Ti^{3+}&AL to TiO_2, a photoanode based on the former gives a 14 times higher photocurrent density than the latter at a bias of 1.25 V vs reversible hydrogen electrode (RHE), suggesting a much lower recombination probability of photogenerated electrons and holes in the former. Moreover, different from the flat step-like photocurrent response patterns to the switching on/off of light in the TiO_2 photoanode, the striking jumps and following decays of the photocurrent in the TiO_2 with Ti^{3+}&AL based photoanode appear at the bias range from around 0 to 0.6 V. This result means that the TiO_2 with Ti^{3+}&AL-based photoanode appears to behave on charging and discharging as does an electronic capacitor. Specifically, the charging process occurs after the light irradiation is applied. This is shown by the rapid decay of the *positive* photocurrent under the irradiation indicated by the red rectangles in Fig. 5b. The discharging process begins after the light irradiation is blocked. The evidence for this is the generation of *negative* current in the dark indicated by the blue rectangles as a result of the refilling of the stored electrical charge (the photoelectrode acts as a photocathode in this stage). On the basis of these features, the stored electrical charge carriers are inferred to be the photogenerated holes. From a comparison of the PEC curves of the two reference photoanodes, TiO_2 with AL and TiO_2 with Ti^{3+} (**Fig. S11**), one can conclude that the observed capacitance property of the TiO_2 with Ti^{3+}&AL photoanode is dominantly controlled by the presence of Ti^{3+} with the amorphous layer as a protecting layer. Moreover, the spatial distribution of Ti^{3+} in the TiO_2 particles plays an important role in determining the capacitance, namely the ability of storing electrical charge. The location of Ti^{3+} in the core favors the storage of holes by blocking the contact of Ti^{3+} with the environmental medium to release the trapped charge. This could be responsible for the much

higher capacitance of TiO_2 with Ti^{3+}&AL than TiO_2 with Ti^{3+} (Fig. S11), where the Ti^{3+} is exposed to the environmental medium.

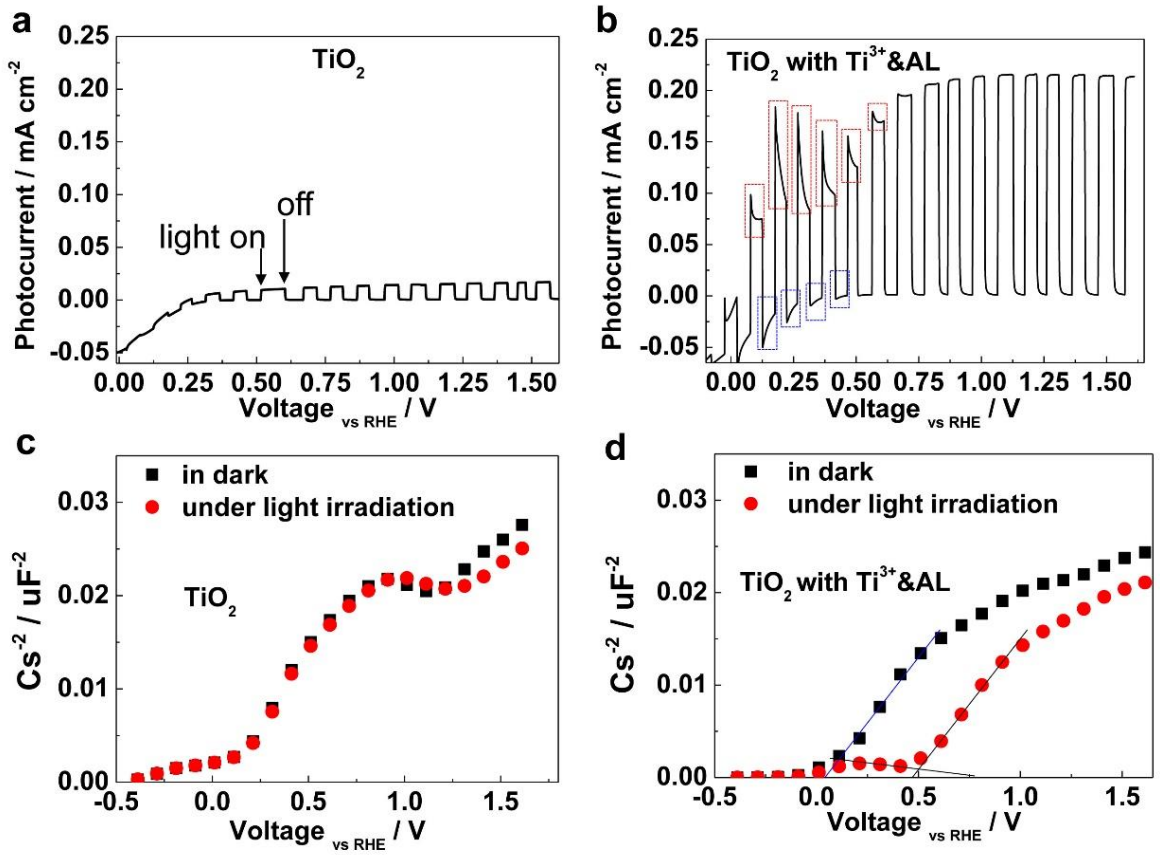

Figure 5 Photoelectrochemical and Mott-Schottky spectroscopy. (**a**, **b**), the applied bias dependent photoelectrochemical water oxidation activity under irradiation with chopped light with the TiO_2 and TiO_2 with Ti^{3+}&AL-based photoanodes in a 0.2 M Na_2SO_4 solution. Scanning rate is 10 mV/s. (**c**, **d**), Mott-Schottky curves of the TiO_2 and TiO_2 with Ti^{3+}&AL based electrodes in the dark and under light irradiation measured in a 0.2 M Na_2SO_4 electrolyte.

The charge storage ability of TiO_2 with Ti^{3+}&AL is further confirmed by the change of its MS curve under light irradiation. In principle, the Fermi level dependent flat band potential of semiconductors, with the ability of storing photogenerated charge, shifts with light excitation according to change in the concentration of charge carriers in the system. Whether a cathodic or anodic shift of the flat band potential occurs depends on the type of charge carriers stored.

The storage of positively charged holes causes anodic shift, as shown in **Fig. 5**d for TiO_2 with Ti^{3+}&AL. Moreover, the plot in the bias range from around 0 to 0.5 V, where the capacitive property was observed (Fig. 5b), gives a positive slope as does a typical cathode. A similar but not so obvious trend was also observed in the TiO_2 with Ti^{3+} based electrode (**Fig. S12a**). In contrast, no shift of the flat band potential upon light irradiation was observed in TiO_2 (Fig. 5c) and TiO_2 with AL (Fig. S12b). These results again confirm the ability to store holes in TiO_2 with Ti^{3+}&AL under light irradiation. Such an ability promotes the separation of photogenerated electrons and holes by efficiently collecting the holes from the bulk and thus reducing recombination in it, which can be further validated by the quenching of radiative recombination of photoexcited electrons and holes in TiO_2 with Ti^{3+}&AL in photoluminence emission spectra (**Fig. S13**). Similar results were also demonstrated in the second-phase modified photoanodes.[26,27]

One prominent feature of amorphous structure as a catalytic reaction platform is its potential abundant surface active sites. Besides the abundance of the active sites, the distribution of reducing and oxidizing active sites plays an important role in affecting the activity of the photocatalysts, which has attracted increasing attention.[28-32] Monitoring the deposition of solid products from the reduction and oxidation reactions induced by the photogenerated electrons and holes (for example, $Au^{3+} + e^- \rightarrow Au$; $Mn^{2+} + h^+ + OH^- \rightarrow MnO_x$) provides a straightforward method for observing the distribution of reducing and oxidizing active sites. **Fig. 6** shows the photodeposition of Au and MnO_x particles on the TiO_2 and TiO_2 with Ti^{3+}&AL photocatalysts. The distinct feature observed is that the surface of the TiO_2 particles is *partially* covered by major Au particles and minor MnO_x particles, but the surface of the TiO_2 with Ti^{3+}&AL particles is *fully* covered by major MnO_x particles and minor Au particles. This fact clearly indicates that only a small fraction of the surface of TiO_2 particles provides catalytic active sites, however, a much larger fraction of the surface of TiO_2 with Ti^{3+}&AL particles provides active sites. Moreover, the surface active sites of TiO_2

mainly consist of reducing reaction sites, while oxidizing reaction sites dominate active sites on the surface of TiO_2 with Ti^{3+}&AL. By further comparing the deposition features of Au and MnO_x particles on the other two reference photocatalysts, TiO_2 with Ti^{3+} and TiO_2 with AL (**Fig. S14**), the co-existence of both an amorphous shell and Ti^{3+} in the crystalline core is concluded to be responsible for the changes in the numbers of reducing and oxidizing active sites on the surface of TiO_2 with Ti^{3+}&AL.

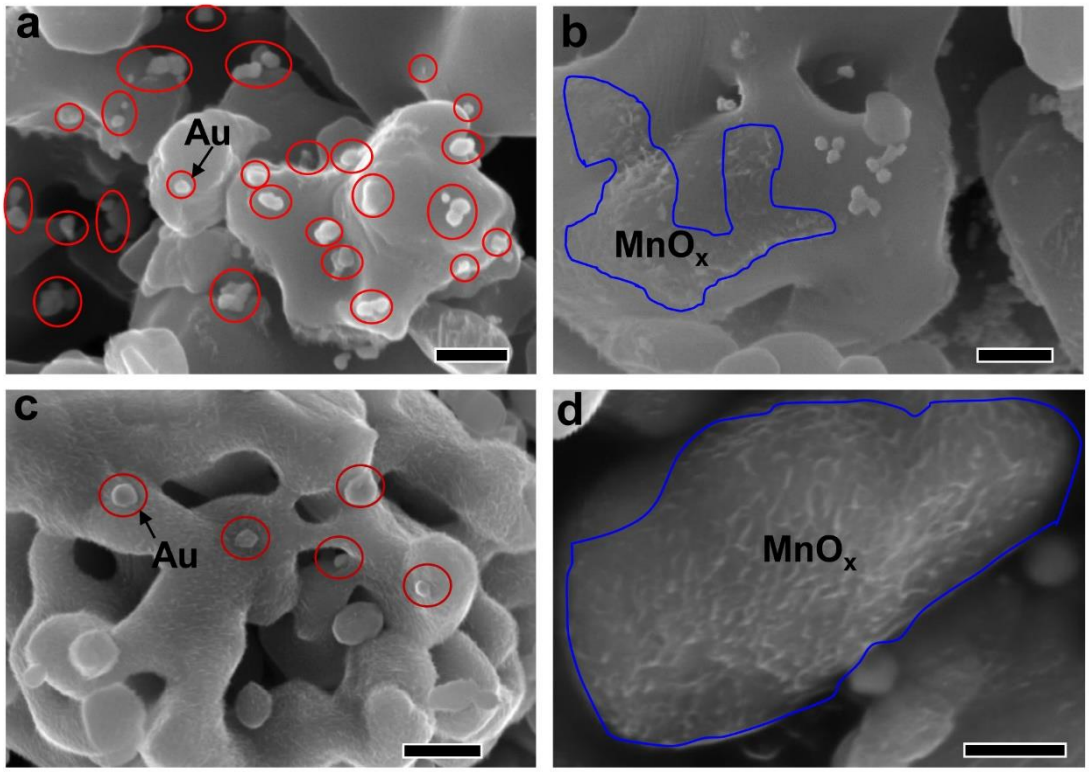

Figure 6 Observations of reducing and oxidizing active sites on photocatalyst particles. (**a**, **b**), Scanning electron microscopy (SEM) images of TiO_2 after simultaneously loading it with Au and MnO_x particles by a photodeposition method; (**c**, **d**), SEM images of TiO_2 with Ti^{3+}&AL after simultaneously loading it with Au and MnO_x particles by a photodeposition method. The distribution of Au and MnO_x particles is marked by red and blue cycles, respectively. Scale bars in (a, b, d) are 250 nm and 500 nm in (c).

The changes in the numbers of reducing and oxidizing sites as a result of the crystalline Ti^{3+} core/amorphous Ti^{4+} shell structure can be understood from the unique band alignments

of TiO_2 with Ti^{3+}&AL. Compared with the band alignments of TiO_2 (Fig. 1a), one most distinctive feature of the band alignments of TiO_2 with Ti^{3+}&AL is the formation of band offsets as a response to the Ti^{3+} related localized states at the bottom of the conduction band (Fig. 1b). The onsets in the conduction and valence bands play opposite roles in affecting the transport of electrons and holes from the bulk to the surface of TiO_2. The upward onset in the conduction band acting as a potential barrier can suppress the transport of electrons from the bulk to the surface, while the upward onset in the valence band reversely facilitates the transport of holes from the bulk to the surface. The electrons can only go cross the amorphous layer through the tunneling effect, as also demonstrated in wide-bandgap amorphous layer passivating narrow-bandgap semiconductor in photoelectrodes[33,34]. As a consequence, the holes have a higher probability of moving from the bulk to the surface than do the electrons, as shown by the dominant distribution of MnO_x particles on the whole surface of the particles (Figs. 6c and d). In contrast, the electrons in TiO_2 have a higher probability of reaching the surface than the holes because of their smaller effective mass determined by the larger slope of the Ti 3*d* than O 2*p* states. This result is confirmed by the dominant distribution of Au particles on the TiO_2 particle surface (Fig. 6a and b). In addition, it is necessary to point out that loading co-catalyst (like Pt in this study) with a larger work function than n-type semiconductor can cause surface band bending upwards of the semiconductor, as examined in TiO_2 or ZnO with RuO_2 co-catalyst[35,36]. This can further favor many more holes reaching surface.

In summary, by creating a crystalline Ti^{3+} core/amorphous Ti^{4+} shell structure, we have successfully activated the inert rutile TiO_2 for high performance photocatalytic hydrogen evolution. The origin of the activation was attributed to the overturned population of surface-reaching holes and electrons enabled by this core/shell structure. Specifically, the unique band alignments originating from the Ti^{3+}-containing crystalline core with the assistance of the Ti^{3+}-free amorphous shell gives rise to the upward onsets at their interface. This design is able

regulate the transport behaviors of holes and electrons from the bulk of a particle to the surface by suppressing the transport of electrons in the conduction band and facilitating the transport of holes in the valence band. We envision that this simple yet effective strategy can be easily extended to the activation other oxide/nitride based photocatalysts for efficient solar energy conversion.

Experimental Section

Preparation of photocatalysts. Commercial rutile TiO_2 (99.8%, Alfa Aesar) was used as the starting material after calcination in air at 700 ^oC for 4 h. Sample *TiO_2 with Ti^{3+}* was obtained by heating rutile TiO_2 at 700 ^oC in a hydrogen atmosphere (purity of H_2: 99.99%) with a flow rate of 50 ml/min for 12 h. Sample *TiO_2 with Ti^{3+}&AL* was obtained by further treating 250 mg of the *TiO_2 with Ti^{3+}* sample in 20 mL of 0.2 M hydrofluoric acid at 200 ^oC for 12 h under hydrothermal conditions. In a control experiment, the reference sample *TiO_2 with AL* was obtained by treating TiO_2 in 20 mL of 0.2 M hydrofluoric acid at 200 ^oC for 12 h under hydrothermal conditions.

(Photo)electrode preparation. Films of rutile TiO_2 particles on fluorine-doped tin oxide (FTO) transparent conductive glass substrates as (photo)electrodes were prepared by the electrophoretic deposition method. In a typical process, 40 mg of the powder sample was suspended in 50 mL of an iodine acetone solution (0.2 g/L) under magnetic stirring. Two pieces of FTO glass substrate with 1 × 2 cm^2 area were immersed in this solution to form a two-electrode system. A bias of 10 V with a DC power supply was applied to drive the deposition of the particles on the substrates for 15 min. The as-deposited film was subjected to the necking process by dropping 20 µl of 10 mM $TiCl_4$ ethanol solution into the films four times and subsequently heating at 350 ^oC for 30 min in air.

Photocatalytic activity measurements. Photocatalytic hydrogen generation reactions were carried out in a top-irradiation vessel connected to a glass gas circulation system. 50 mg of the

photocatalyst powder was dispersed in a 300 mL aqueous solution containing 30 mL methanol. The deposition of 1 wt% Pt was achieved by dissolving H_2PtCl_6 in 300 mL of this reaction solution. The reaction temperature was kept around 10 ^oC. The amount of H_2 generated was determined using a gas chromatograph (Agilent 6890N). The light source was a 300 W Xe lamp (Beijing Trusttech Co. Ltd, PLS-SXE-300UV).

*Photoelectrochemical measurements***.** Measurements were conducted in a quartz cell with a conventional three-electrode system. The working electrode, counter electrode and reference electrode were TiO_2 photoelectrode, Pt foil, Ag/AgCl electrode, respectively. The electrolyte was a 0.2 M Na_2SO_4 aqueous solution. Light irradiation was under AM 1.5G illumination (Newport) with a density of 100 mW cm^{-2}. The photoanode surface area illuminated was 1 cm^2, and the scanning rate was 10 mV s^{-1}. The measured potentials vs the RHE scale can be obtained from the potentials vs Ag/AgCl using the Nernst equation (E_{RHE} = $E_{Ag/AgCl}$ +0.059pH + 0.196).

Characterization. X-ray diffraction patterns were recorded on a Rigaku diffractometer using Cu Kα irradiation. The compositions and chemical states of the samples were analyzed using X-ray photoelectron spectroscopy (Thermo Escalab 250, with a monochromatic Al K α X-ray source). All binding energies were referenced to the C 1s peak (284.6 eV) that arises from adventitious carbon. The optical absorption spectra were measured on a UV-visible spectrophotometer (JASCO-550) in the diffuse reflectance mode. Photoluminescence emission spectra (390 nm excitation) were measured at room temperature with a fluorescence spectrophotometer (Edinburgh Instruments, FLSP-920). Electron spin resonance spectra were measured at room temperature using a JEOL JES-FA200 ESR spectrometer. Mott-Schottky curves were recorded on a PARSTAT 2273 electrochemical workstation (Princeton Applied Research). The Mott–Schottky plots were obtained at an AC frequency of 1 kHz in a 0.2 M Na_2SO_4 aqueous electrolyte. Light irradiation was under AM 1.5G illumination (Newport) with a density of 100 mW cm^{-2}.

Supporting Information

Supporting Information is available from the Wiley Online Library or from the author.

Acknowledgements

The authors thank the Major Basic Research Program, Ministry of Science and Technology of China (2014CB239401), NSFC (Nos. 51422210, 51572266, 51561130157, 51172243, 51521091). GL thanks Newton Advanced Fellowship.

Received: ((will be filled in by the editorial staff))
Revised: ((will be filled in by the editorial staff))
Published online: ((will be filled in by the editorial staff))

[1] A. L. Linsebigler, G. Q. Lu, J. T. Yates, *Chem. Rev.*, **1995**, *95*, 735-758.

[2] H. Tada, T. Kiyonaga, S. Naya, *Chem. Soc. Rev.*, **2009**, *38*, 1849-1858.

[3] A. Kudo, Y. Miseki, *Chem. Soc. Rev.*, **2009**, *38*, 253-278.

[4] J. Tao, T. Luttrell, M. Batzill, *Nat. Chem.*, **2011**, *3*, 296-300.

[5] L. Liu, & X. Chen, *Chem. Rev.*, **2014**, *114*, 9890-9918.

[6] L. Thulin, J. Guerra, *Phys. Rev. B*, **2008**, *77*, 195112.

[7] G. Hautier, A. Miglio, G. Ceder, G. M. Rignanese, X. Gonze, *Nat. Commun.*, **2013**, *4*, doi:10.1038/ncomms3292.

[8] M. Yoshida, T. Hirai, K. Maeda, N. Saito, J. Kubota, H. Kobayashi, Y. Inoue, K. Domen, *J. Phys. Chem. C*, **2010**, *114*, 15510-15515.

[9] M. N. Huda, Y. F. Yan, S. H. Wei, M. M. Al-Jassim, *Phys. Rev. B*, **2008**, *78*, 195204.

[10] J. H. Yang, D. G. Wang, H. X. Han, C. Li, *Acc. Chem. Res.*, **2013**, *46*, 1900-1909.

[11] L. Chen, J. H. Yang, S. Klaus, L. J. Lee, R. Woods-Robinson, J. Ma, Y. Lum, J. K. Cooper, F. M. Toma, L. W. Wang, I. D. Sharp, A. T. Bell, J. W. Ager, *J. Am. Chem. Soc.*, **2015**, *137*, 9595-9603.

[12] C. Wu, X. Lu, L. Peng, K. Xu, X. Peng, J. Huang, G. Yu, Y. Xie, *Nat. Commun.*, **2015**, *4*, doi: 10.1038/ncomms9647.

[13] G. Liu, H. G. Yang, J. Pan, Y. Q. Yang, G. Q. Lu, H. M. Cheng, *Chem. Rev.*, **2014**, *114*, 9559-9612.

[14] X. B. Chen, L. Liu, P. Y. Yu, S. S. Mao, *Science*, **2011**, *331*, 746.

[15] Y. H. Hu, *Angew. Chem. Int. Ed.*, **2012**, *51*, 12410.

[16] B. Han, W. Wei, L. Chang, P. F. Cheng, Y. H. Hu, *ACS catal.*, **2016**, *6*, 494.

[17] T. Simon, N. Bouchonville, M. J. Berr, A. Vaneski, A. Adrovic, D. Volbers, R. Wyrwich, M. Doeblinger, A. S. Susha, A. L. Rogach, F. Jackel, J. K. Stolarczyk, J. Feldmann, *Nat. Mater.*, **2014**, *13*, 1013-1018.

[18] G. Liu, H. G. Yang, X. W. Wang, L. N. Cheng, H. F. Lu, L. Z. Wang, G. Q. Lu, H. M. Cheng, *J. Phys. Chem. C*, **2009**, *113*, 21784-21788.

[19] J. C. Yu, J. G. Yu, W. K. Ho, Z. T. Jiang, L. Z. Zhang, *Chem. Mater.*, **2002**, *14*, 3808-3816.

[20] T. Berger, O. Diwald, E. Knoezinger, F. Napoli, M. Chiesa, E. Giamello, *Chem. Phys.*, **2007**, *339*, 138-145.

[21] S. Hoang, S. P. Berglund, N. T. Hahn, A. J. Bard, C. B. Mullins, *J. Am. Chem. Soc.*, **2012**, *134*, 3659-3662.

[22] A. K. Ghosh, F. G. Wakim, R. R. Addiss, *Phys. Rev.*, **1969**, *184*, 979-988.

[23] Y. Mi, Y. X. Weng, *Sci. Rep.*, **2015**, *5*, doi:10.1038/srep11482.

[24] T. Kawahara, Y. Konishi, H. Tada, N. Tohge, J. Nishii, S. Ito, *Angew. Chem. Int. Ed.*, **2002**, *41*, 2811-2813.

[25] C. Zhen, L. Z. Wang, L. Liu, G. Liu, G. Q. Lu, H. M. Cheng, *Chem. Commun.*, **2013**, *49*, 6191-6193.

[26] G. J. Liu, J. Y. Shi, F. X. Zhang, Z. Chen, J. F. Han, C. M. Ding, S. S. Chen, Z. L. Wang, H. X. Han, C. Li, *Angew. Chem. Int. Ed.*, **2014**, *53*, 7295-7299.

[27] W. Jiarui, F. E. Osterloh, *J. Mater. Chem. A*, **2014**, *2*, 9405-9411.

[28] T. Ohno, K. Sarukawa, M. Matsumura, *New J. Chem.*, **2002**, *26*, 1167-1170.

[29] R. G. Li, F. X. Zhang, D. G. Wang, J. X. Yang, M. R. Li, J. Zhu, X. Zhou, H. X. Han, C. Li, *Nat. Commun.*, **2013**, *4*, doi:10.1038/ncomms2401.

[30] C. Liu, X. G. Han, S. F. Xie, Q. Kuang, X. Wang, M. S. Jin, Z. X. Xie, L. S. Zheng, *Chem. Asian J.*, **2013**, *8*, 282-289.

[31] C. Zhen, J. C. Yu, G. Liu, H. M. Cheng, *Chem. Commun.*, **2014**, *50*, 10416-10419.

[32] T. Tachikawa, S. Yamashita, T. Majima, *J. Am. Chem. Soc.*, **2011**, *133*, 7197-7204.

[33] J. C. Hill, A. T. Landers, J. A. Switzer, *Nat. Mater.*, **2015**, *14*, 1150.

[34] A. G. Scheuermann, J. P. Lawrence, K. Kemp, T. Ito, A. Walsh, C. E. D. Chidsey, P. K. Hurley, P. C. McIntyre, *Nat. Mater.*, **2016**, *15*, 99.

[35] M. T. Uddin, Y. Nicolas, C. Olivier, T. Toupance, M. M. Müller, H. J. Kleebe, K. Rachut, J. Ziegler, A. Klein, W. Jaegermann, *J. Phys. Chem. C*, **2013**, *117*, 22098.

[36] M. T. Uddin, Y. Nicolas, C. Olivier, L. Servant, T. Toupance, S. Li, A. Klein, W. Jaegermann, *Phys. Chem. Chem. Phys.*, **2015**, *17*, 5090.